

Entanglement of Trapped-Ion Clock States

P. C. Haljan, P. J. Lee, K.-A. Brickman, M. Acton, L. Deslauriers, C. Monroe
FOCUS Center and University of Michigan Department of Physics
 (Dated: 13 Aug 2005)

A Mølmer-Sørensen entangling gate is realized for pairs of trapped $^{111}\text{Cd}^+$ ions using magnetic-field insensitive “clock” states and an implementation offering reduced sensitivity to optical phase drifts. The gate is used to generate the complete set of four entangled states, which are reconstructed and evaluated with quantum-state tomography. An average target-state fidelity of 0.79 is achieved, limited by available laser power and technical noise. The tomographic reconstruction of entangled states demonstrates universal quantum control of two ion-qubits, which through multiplexing can provide a route to scalable architectures for trapped-ion quantum computing.

PACS numbers: 03.67.Mn, 03.65.Wj, 03.65.Ud, 32.80.Pj

Entangled states such as the famous EPR-Bohm states [1, 2] have long been of interest in the interpretation of quantum mechanics [3]; however, their generation has become a rapidly growing field with the recognition of entanglement as a powerful resource for quantum information processing[4]. Laser-addressed trapped ions with qubits embedded in long-lived internal hyperfine levels hold significant advantages for quantum information applications [5, 6]. A critical issue is the robust generation of scalable entanglement. In the context of trapped ions this is reduced to the problem of two-qubit entanglement, as plausible multiplexing schemes have been proposed to create a scalable architecture for a quantum processor[7, 8].

Trapped-ion entangling gates mediated by phonons of the collective ion motion are susceptible to various forms of noise - qubit and motional decoherence, impure initial conditions, and technical issues associated with the optical Raman lasers driving the gate[5]. Robust schemes for gates based on spin-dependent forces have been proposed [9, 10, 11, 12] and experimentally implemented [13, 14] that, for example, relax the purity requirement on the initial motional state of the ions. Here we report the realization of one such entangling gate for pairs of trapped $^{111}\text{Cd}^+$ ions that uses an advantageous implementation[15, 16] of the Mølmer-Sørensen (MS) scheme[9, 13]. The implementation reduces sensitivity to optical phase drifts through an appropriate Raman beam setup and reduces sensitivity to magnetic field fluctuations through the use of magnetic-field insensitive clock states[17].

Quantum state tomography [18, 19, 20, 21] is used to characterize the gate performance for the creation of all four entangled Bell-like states. Previous applications of quantum state tomography with ions include the reconstruction of non-classical states of motion [22, 23, 24] as well as entangled states of optical ion-qubits composed of electronic levels [20]. Here we present the first such implementation for hyperfine qubits, in the process demonstrating universal quantum control of two clock-state ion-qubits.

The MS gate for two trapped ions is based on optical Raman couplings to the first vibrational sidebands of the ions’ collective motion, assumed along the z -axis. The ions are equally illuminated by a bichromatic Raman field inducing simultaneous red and blue sideband interactions [22] that couple each ion’s spin to the vibrational levels $\{|n\rangle\}$ of a single collective mode of motion - stretch or center of mass [Fig. 1(a)]. With the Raman fields far detuned from the sidebands, negligible direct coupling occurs; however, the fields can combine to provide a resonant two-step coupling between for example $|\downarrow\downarrow\rangle$ and $|\uparrow\uparrow\rangle$, generating the entangled state $1/\sqrt{2}(|\downarrow\downarrow\rangle + i|\uparrow\uparrow\rangle)$ [Fig. 1(a)]. In general, the bichromatic field provides an entangling gate based on a nonlinear two-qubit interaction such as $H = -\hbar\tilde{\Omega}(\hat{\sigma}_x \otimes \hat{\sigma}_x)/2$, written in terms of Pauli operators. The coupling strength $\tilde{\Omega}$, which in the Lamb-Dicke limit is independent of the initial value of $|n\rangle$, is given by $(\eta\Omega)^2/\delta$ where Ω is the carrier Rabi frequency and δ the detuning. The Lamb-Dicke parameter $\eta = kz_0$ for the motional mode of interest is character-

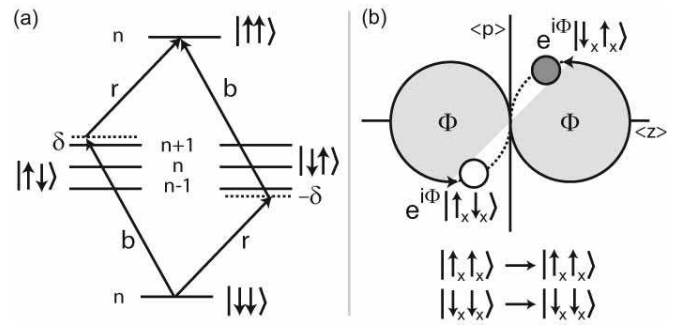


FIG. 1: Two views of the Mølmer-Sørensen $\hat{\sigma}_x \otimes \hat{\sigma}_x$ entangling gate for two ions in (a) energy space [9] and (b) motional phase space [14] for the gate-diagonal spin basis. The quantum number n and phase-space co-ordinates describe a given collective motional mode. Red and blue Raman sideband couplings are labeled by r and b and have detuning $\delta_b = \delta = -\delta_r$. For a closed phase-space trajectory, the phase Φ depends only on the area enclosed.

ized by Raman wavevector difference k along the z -axis of motion and zero-point wavepacket size $z_o = \sqrt{\hbar/2M\omega}$, where ω and M are the frequency and total mass of the excitation respectively.

Reducing the detuning δ accelerates the gate speed at the expense of populating intermediate motional states [25]. In this situation it is more natural to view the bichromatic field as generating a spin-dependent force constructed from red and blue sideband couplings with balanced Rabi frequencies and detunings [15, 16, 26]. The resulting interaction on each ion is equivalent to $H \sim \hat{\sigma}_x z F_o \sin \omega_d t$ describing a $\hat{\sigma}_x$ -dependent force near resonance ($\omega_d = \omega + \delta$) with strength $F_o z_o = \eta\Omega$. The total Hamiltonian is the sum of interactions on each ion. For a force resonant with the stretch mode and acting in-phase on the two ions, the time-evolution operator can be expressed in the $\hat{\sigma}_x$ -diagonal gate basis as a spin-dependent displacement as follows:

$$\begin{aligned} \hat{U}(t) = & |\uparrow_x \uparrow_x\rangle \langle \uparrow_x \uparrow_x| + |\downarrow_x \downarrow_x\rangle \langle \downarrow_x \downarrow_x| \\ & + e^{-i\Phi} \hat{D}(\alpha) |\uparrow_x \downarrow_x\rangle \langle \uparrow_x \downarrow_x| + e^{-i\Phi} \hat{D}(-\alpha) |\downarrow_x \uparrow_x\rangle \langle \downarrow_x \uparrow_x| \end{aligned} \quad (1)$$

where $\hat{D}(\alpha)$ is the displacement operator in the phase space of the driven normal mode [Figure 1(b)]. The value of the displacement is $\alpha(t, \delta) = \alpha_o(1 - e^{-i\delta t})$ and the corresponding phase accumulated over the trajectory is $\Phi(t, \delta) = \alpha_o^2(\delta t - \sin \delta t)$ in terms of the parameter $\alpha_o = \eta\Omega/\delta$. In general, the spin-dependent displacement entangles the spin and motional degrees of freedom; however, for a closed trajectory ($\delta t = 2\pi m$, m an integer), the spin and motion disentangle leaving only a spin-dependent geometric phase $\Phi_g = 2\pi m(\eta\Omega/\delta)^2$ applied to the gate basis. A maximally entangling phase gate is constructed from a geometric phase of $\pi/2$. We achieve this in the fastest time possible with $m=1$ requiring detuning $\delta = 2\eta\Omega$ and gate time $\tau_g = 2\pi/\delta$. Expressed in the computational basis, the MS gate structure, although slightly more complicated, makes the entangling action manifest:

$$\begin{aligned} |\uparrow\uparrow\rangle &\rightarrow \Psi_1 = \frac{1}{\sqrt{2}} (|\uparrow\uparrow\rangle + ie^{i\phi_e} |\downarrow\downarrow\rangle) \\ |\downarrow\downarrow\rangle &\rightarrow \Psi_2 = \frac{1}{\sqrt{2}} (|\downarrow\downarrow\rangle + ie^{-i\phi_e} |\uparrow\uparrow\rangle) \\ |\uparrow\downarrow\rangle &\rightarrow \Psi_3 = \frac{1}{\sqrt{2}} (|\uparrow\downarrow\rangle + ie^{i\phi_o} |\downarrow\uparrow\rangle) \\ |\downarrow\uparrow\rangle &\rightarrow \Psi_4 = \frac{1}{\sqrt{2}} (|\downarrow\uparrow\rangle + ie^{-i\phi_o} |\uparrow\downarrow\rangle) \end{aligned} \quad (2)$$

The phases ϕ_o and ϕ_e have been included in the even and odd parity states, $\Psi_{1,2}$ and $\Psi_{3,4}$ respectively, to account for the effect of both ac Stark shifts and Raman laser coherences, the latter modifying the spin dependence of the gate [16, 27]. For $\phi_e = \phi_o = 0$, the gate's action reduces to that of a $\hat{\sigma}_x \otimes \hat{\sigma}_x$ coupling.

Our qubit resides in the hyperfine clock states $|\uparrow\rangle = |F=0, m_F=0\rangle$ and $|\downarrow\rangle = |F=1, m_F=0\rangle$ of a $^{111}\text{Cd}^+$ ion with frequency separation $\omega_{hf}/2\pi = 14.53\text{GHz}$ and second-order Zeeman shift $600\text{Hz}/\text{G}^2$ near zero magnetic field. A pair of ions, confined in a three-layer linear Paul

trap [28] is aligned along the weak z -axis. The ions' secular harmonic motion in the z -direction is characterized by center-of-mass and stretch normal modes with frequencies $\omega_c = 2.05\text{MHz}$ and $\omega_s = \sqrt{3}\omega_c$. All requirements for arbitrary two-qubit control are implemented as follows. Both modes of motion are initialized to near their ground state ($\bar{n}_c \sim 0.4, \bar{n}_s \sim 0.2$) with 60 pulses of Raman sideband cooling [28]. Due to the simplicity of the hyperfine structure (nuclear spin $I = 1/2$), the qubits are directly initialized with optical pumping to $|\uparrow\rangle$. Following coherent operations the qubits can be read out with high fidelity using a photomultiplier tube (PMT) allowing $|\uparrow\uparrow\rangle, |\downarrow\downarrow\rangle$ and $\{|\uparrow\downarrow\rangle, |\downarrow\uparrow\rangle\}$ to be distinguished by virtue of state-dependent fluorescence [6]. Unambiguous readout of all four qubit states, in particular $|\uparrow\downarrow\rangle$ and $|\downarrow\uparrow\rangle$, is achieved with an intensified CCD camera that can independently and simultaneously image the fluorescence collected from each ion-qubit. A camera detection fidelity of 97% is achieved in 15ms limited by readout electronics.

Coherent single qubit operations are achieved through a combination of applied microwave fields and ion-selective ac Stark shifts. Resonant microwaves provide simultaneous Rabi flopping of both qubits with a Rabi frequency of 56kHz. Arbitrary *independent* qubit rotations are achieved by combining microwave operations with pulses of an off-resonant laser beam 200GHz detuned from resonance. The laser beam with moderate waist ($\lesssim 10\mu\text{m}$ compared with the $2.5\mu\text{m}$ ion spacing) is aligned to be off-center with respect to the two ions, giving rise to an intensity gradient and differential ac Stark shift between the two ions. A $10\mu\text{s}$ exposure results in a phase shift difference between the two qubits of approximately $\pi/2$.

The MS entangling gate is achieved using a pair of Raman laser beams 200GHz detuned from optical resonance. An electrooptic modulator (EOM) at microwave frequency together with an acousto-optic modulator in each Raman beam provide the required bichromatic Raman beatnote [29]. The collective stretch mode is chosen for gate implementation due to the significantly suppressed heating rate [30]. The stretch sideband Rabi frequency is typically 6kHz. The wavevectors of the red and blue Raman fields are arranged in a counter-propagating geometry so that the spin coherence of the MS gate, included in ϕ_e , is insensitive to optical phase drifts between the Raman beams [15, 16]. Although this setup requires an accurate ion spacing to maximize gate speed, the stability of the spin coherence is crucial for keeping the MS gate synchronized with the microwave fields during tomography. A noise eater, stabilizing the Raman beam power, is used to suppress the effect of fluctuating ac Stark shifts (where the average qubit shift is 75kHz compared with 13kHz gate speed as discussed below).

The sequence to implement the gate begins with balancing the sideband strengths to better than 10% and the

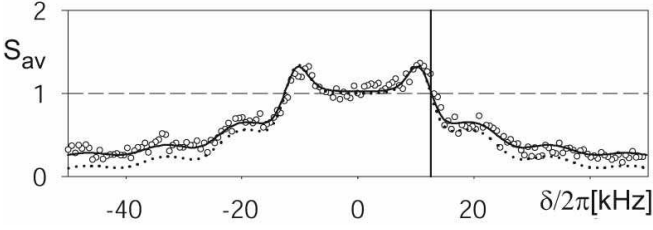


FIG. 2: Average brightness S_{av} (see text) versus MS gate detuning δ . Applied gate time ($75\mu\text{s}$) is within 10% of the ideal. Dotted line indicates expected signal modified to include an initial temperature $\bar{n}_s = 0.3$ [15]. Solid line is a fit including offset and contrast factors to account for imperfections such as spontaneous emission. The fit gives a sideband Rabi frequency $\eta\Omega/2\pi = 6.3\text{kHz}$ and initial stretch mode temperature $\bar{n}_s = 0.3$. Vertical line shows ideal gate operation point $\delta = 2\eta\Omega$, roughly at $S_{av} = 1$. Each point is the average of 150 PMT measurements.

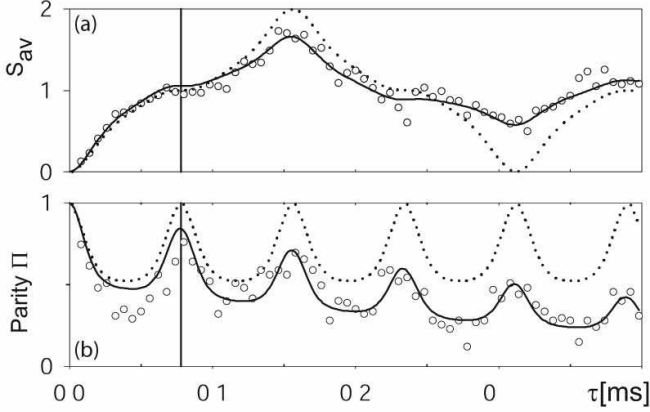


FIG. 3: Time scan of MS gate showing (a) average brightness S_{av} and (b) parity Π . Ideal gate evolution shown as dotted lines with best fit including exponential damping shown with solid line. The fit gives a sideband Rabi frequency $\eta\Omega/2\pi = 6.6\text{kHz}$ and detuning $\delta/2\pi = 12.8\text{kHz} \approx 2\eta\Omega/2\pi$ with other parameters the same as in figure 2. Vertical line shows gate operation time $\tau = 2\pi/\delta \approx 80\mu\text{s}$.

detunings to $\sim 100\text{Hz}$. Applying the bichromatic field for time τ to the initial state $|\uparrow\uparrow\rangle$ while scanning the detuning δ pinpoints the required gate detuning to near $2\eta\Omega$ [Fig. 2]. The dynamics of the frequency scan can be understood in terms of the evolution of entangled states of spin and motion [14, 15]. Assuming the initial spin state $|\uparrow\uparrow\rangle$ and motional ground state $|n_s=0\rangle$, the average ion brightness defined as $S_{av} = 2P_{\downarrow\downarrow} + P_{\uparrow\downarrow} + P_{\downarrow\uparrow}$ is $S_{av}(\tau, \delta) = 1/2(1 + \cos \Phi(\tau, \delta)e^{-|\alpha(\tau, \delta)|^2/2})$. With the detuning now fixed, the average brightness is monitored while scanning the gate time. The time evolution reveals the overall spin dynamics modulated by faster dynamics associated with the phase-space evolution [Fig. 3(a)]. Each location of zero slope corresponds to the ion mo-

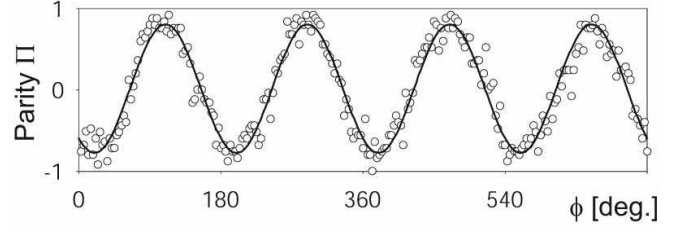


FIG. 4: Parity versus phase of analysis $\pi/2$ pulse applied to the Ψ_1 state. The solid line is a sinusoidal fit yielding an amplitude $0.79(2)$. The fidelity of the state shown is $0.83(2)$. Each point is an average over 50 PMT measurements and other parameters are as in text.

tion returning on itself to form a closed trajectory. The return points are most clearly visualized in the parity signal, $\Pi = (P_{\uparrow\uparrow} + P_{\downarrow\downarrow}) - (P_{\uparrow\downarrow} + P_{\downarrow\uparrow}) = 1/2(1 + e^{-2|\alpha(\tau, \delta)|^2})$ [Fig. 3(b)]. At the gate operation time ($80\mu\text{s}$), corresponding to the first return, the initial state $|\uparrow\uparrow\rangle$ has evolved ideally to $\Psi_1 = 1/\sqrt{2}(|\uparrow\uparrow\rangle + ie^{i\phi_e}|\downarrow\downarrow\rangle)$.

The simplest indicator for the quality of the entangled states formed is the fidelity $F = \langle \Psi | \rho | \Psi \rangle$ with which the actual density matrix ρ matches the target state Ψ . The fidelity for creating the Bell-like states of Eqn. 2 is simply the sum of the two relevant diagonal population terms of ρ and the corresponding pair of off-diagonal coherences. It is easy to directly extract the coherences for the even parity states $\Psi_{1,2}$ without single-qubit operations. A single global $\pi/2$ analysis pulse is applied to the state; varying the phase of the analysis pulse yields an oscillating parity signal [Fig. 4] with amplitude equal to twice the off-diagonal coherence [13, 31]. For the case of Ψ_1 as shown in Fig. 4, a typical fidelity of 0.80 is achieved (which must exceed 0.5 to achieve entanglement [13, 32]).

A full evaluation of the entangled state including a quantitative measure of the entanglement requires access to the full density matrix, in particular all the off-diagonal coherences. To determine the fifteen free parameters for a normalized two-qubit density matrix requires at least as many independent measurements. We follow closely the tomographic approach outlined in refs. [19, 21]. The density matrix can be decomposed in terms of a tensor product basis $\rho = \sum_{i,j=0}^3 r_{ij} \sigma_i \otimes \sigma_j$ where $\sigma_0 \equiv \mathbb{I}$, $\sigma_1 \equiv \sigma_x$, $\sigma_2 \equiv \sigma_y$ and $\sigma_3 \equiv \sigma_z$ are the usual single-qubit Pauli matrices satisfying $\text{Tr}(\sigma_i \sigma_j) = 2\delta_{ij}$, and $r_{ij} = \text{Tr}(\rho \sigma_i \otimes \sigma_j)$ are real numbers. In the experiment we choose to perform projective measurements in the nine basis combinations $\{\sigma_i \otimes \sigma_j, i, j = x, y, z\}$ each yielding four possible outcomes for a total of twenty-seven independent measurements accounting for normalization. The fluorescence measurement accesses σ_z projections. To implement transverse $\sigma_{x,y}$ projections, we make use of independent single-qubit rotations to transform into the σ_z basis before measurement. Repeated preparation

of a target state followed by tomographic measurement is performed for 200 shots per measurement basis. The total reconstruction time takes about 60s, dominated by the cooling cycle and camera readout time.

A fast, direct inversion for the density matrix can be made with a minimum complete measurement set of fifteen values r_{ij} . However, this process in general leads to an unphysical density matrix due to experimental error. Instead, maximum likelihood estimation is used to fit the data to a density matrix form constrained to be Hermitian, normalized and positive semidefinite. The inclusive and mutually exclusive nature of the four measurement outcomes for each basis is taken into account by least-squares weighting according to a multinomial distribution [33]. Systematics of the tomographic process are assessed after the fact based on tomographic control runs of input states $|\uparrow\uparrow\rangle$ and $|\downarrow\downarrow\rangle$ assumed to be ideal. The results from the controls are used to extract detection biases (on the order of a few percent), microwave Rabi frequency and applied ac Stark shifts used for qubit rotations. Statistical errors for parameters calculated from the reconstructed density matrix are difficult to extract directly and so are obtained using a simple numerical bootstrap method [34]. The raw shot-by-shot data are randomly resampled with replacement to generate successive data sets from which a distribution of a parameter's value can be obtained.

All four Bell-like entangled states are created according to Eqn. 2 by applying the MS gate to the different computational states. Figure 5 shows their reconstructed density matrices. The inferred fidelities for the target states Ψ_1 through Ψ_4 are $F = \{0.82(3), 0.89(3), 0.78(3), 0.66(3)\}$ where the phases $\phi_e = -1.1\text{rad}$ and $\phi_o = 0.43\text{rad}$ are considered free parameters obtained from the fits. The tomographically obtained fidelity for Ψ_1 agrees well with a simple parity-based assessment like that discussed above. The fidelity for creating the odd-parity states $\Psi_{3,4}$ is worse because of inaccurate preparation of the input states $|\uparrow\downarrow\rangle$ and $|\downarrow\uparrow\rangle$ ($F \approx 0.85$). Accounting for this factor, the fidelities of all states are on par.

Inseparability (entanglement) of the reconstructed two-qubit states can be tested by performing a partial transpose of the density matrix and searching for a negative value in the resultant eigenvalue spectrum [35, 36]. For example, the eigenvalue spectrum obtained for the Ψ_2 case is $\{-0.42(3), 0.40(3), 0.49(2), 0.53(2)\}$ compared with the ideal case $\{-0.5, 0.5, 0.5, 0.5\}$. The negativity N [37, 38], twice the absolute value of the negative eigenvalue, is obtained for all four target states Ψ_i with values $N = \{0.74(6), 0.84(7), 0.60(5), 0.42(6)\}$. Ranging from zero for a separable state to one for a maximally entangled one, the value gives an indication of the degree of the entanglement. Several quantitative measures of entanglement exist in the literature [39], although lacking a closed form they are in general difficult to calculate. One standard measure that is directly calculable

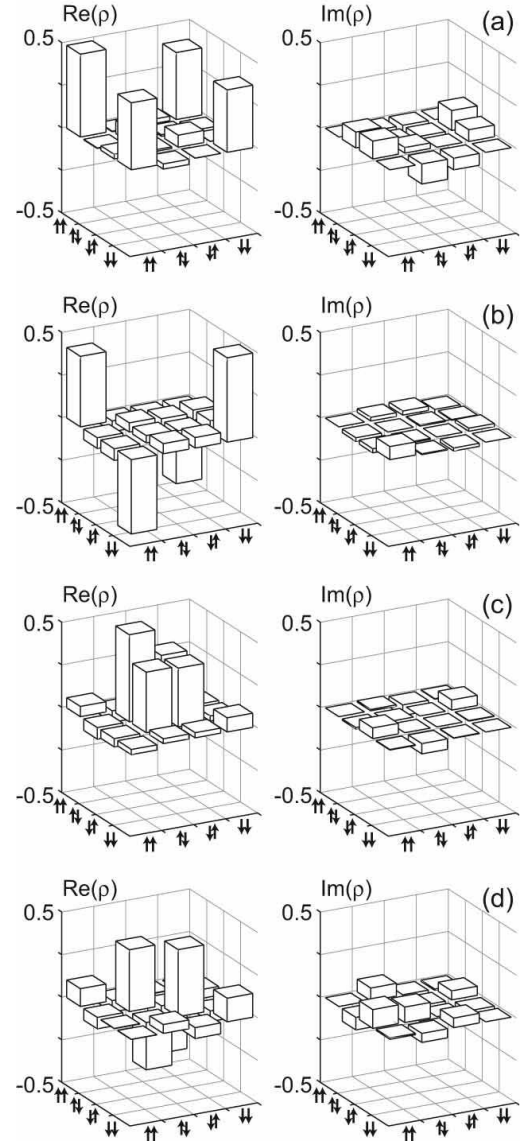


FIG. 5: Tomographically reconstructed density matrices (a)–(d) for the four Bell-like entangled states Ψ_1 through Ψ_4 as per Eqn. 2. To allow direct comparison of diagonal and off-diagonal elements, the reconstructed matrices were rotated into the real co-ordinate using fit parameter $\phi_e = -1.1\text{rad}$ for (a) and (b), and $\phi_o = 0.43\text{rad}$ for (c) and (d). Each state reconstruction uses 27 independent projective camera measurements averaged over 200 runs.

for two qubits is the entanglement of formation E_F [40] again ranging from zero for a separable state to one for a maximally entangled one. In the context of pure states, the value of E_F can be interpreted as the number nE_F of maximally entangled states required to reconstruct n copies of a given state [32]. The experimental values for the four states shown in Fig. 5 are $E_F = \{0.65(8), 0.77(9), 0.49(6), 0.32(6)\}$. The entanglement of formation is a manifestly more strict indicator for the quality of an

entangled state than the fidelity and drops quickly with decreasing fidelity.

Among the experimental sources of gate imperfection, spontaneous emission and fluctuating ac Stark shifts stand out as the likely primary sources of the observed infidelity. For our setup, the gate speed ($\Omega_g = 2\pi/\tau_g = 2\eta\Omega$), which is proportional to the stimulated Raman Rabi frequency Ω , scales as $I\gamma^2/\Delta$ in terms of the optical linewidth $\gamma/2\pi = 60\text{MHz}$, the Raman laser intensity I and its detuning Δ (not to be confused with the detuning δ of the net two-photon Raman transition). In addition to generating the desired gate action, the Raman beams are responsible for a spontaneous scattering rate γ_{sc} per ion and residual differential ac Stark shift $\delta\nu_{st}$ of the hyperfine qubit levels. The probability of a spontaneous photon being scattered during a gate operation is $p_{sc} = 2\gamma_{sc}\tau_g = 2\beta\gamma/\Delta$ where the factor of two accounts for the presence of two ions. A rough theoretical estimate can be made for the prefactor $\beta = \sqrt{2\pi}/\epsilon\zeta\eta \approx 400$, which includes a $\sqrt{2}$ factor accounting for the bichromatic field, a factor $\epsilon \sim 0.2$ characterizing the EOM Raman transition efficiency[29], a Clebsch-Gordon related factor $\zeta = 0.5$ and the Lamb-Dicke parameter $\eta = 0.1$ for the stretch mode. Similarly, the ac Stark phase acquired during a gate is $\phi_{st} = \delta\nu_{st}\tau_g = \beta\omega_{hf}/\Delta$. The relatively large value of $\omega_{hf}/2\pi = 14.5\text{GHz}$ for Cd^+ , while useful for high fidelity qubit detection, requires a significant detuning Δ to suppress Stark shifts. Experimentally, for our modest detuning $\Delta/2\pi \approx 200\text{GHz}$ we measure a value of $\delta\nu_{st}/2\pi = 75\text{kHz}$, from which we obtain $\phi_{st} = 12\pi$ and infer $p_{sc} \approx 0.3$. The value of p_{sc} agrees roughly with the direct theoretical estimate and predicts an infidelity $1 - F \approx 0.73p_{sc} = 0.2$, roughly in agreement with the observed value for creating $\Psi_{1,2}$. The factor of 0.73 appears in the infidelity since a spontaneous scattering event will result in a mixed state that still has some residual overlap with the entangled target state.

Increasing the detuning Δ can reduce the relative effect of both spontaneous emission and Stark shift (see also ref. [41]); however, a concomitant increase in the power of the Raman beams is required to maintain the speed of the entangling gate (and Raman cooling), thereby avoiding slower sources of noise such as magnetic field drift or laser beam-steering noise. In the short term, a reasonable increase in Raman laser detuning and power (currently $\sim 1\text{mW}$) by a factor of ten would reduce the spontaneous emission and sensitivity to ac Stark shifts by the same amount. Ultimately detunings on the order of the large fine structure (74THz) of Cd^+ [29] allow for significant suppression of both effects (see also ref. [42]).

In conclusion, a Mølmer-Sørensen gate has been realized to generate pair-wise entanglement of clock-state ion-qubits with reduced sensitivity to interferometric phase fluctuations of the Raman beams. The tomographic reconstruction used to assess the resultant entangled states demonstrates universal two-qubit control,

which is being directly applied to investigate prototype quantum algorithms [43].

This work is supported by the National Security Agency and Advanced Research and Development Activity under Army Research Office contract W911NF-04-1-0234, and the National Science Foundation Information Technology Research program.

-
- [1] A. Einstein, B. Podolsky, and N. Rosen, *Phys. Rev.* **47**, 777 (1935).
 - [2] D. Bohm, *Quantum Theory* (Dover, 1979).
 - [3] J. Bell, *Speakable and Unspeakable in Quantum Mechanics* (Cambridge Univ. Press, 2004), 2nd ed.
 - [4] M. A. Nielsen and I. L. Chuang, eds., *Quantum Computation and Quantum Information* (Cambridge Univ. Press, 2000).
 - [5] D. J. Wineland *et al.*, *J. Res. Nat. Inst. Stand. Tech.* **103**, 259 (1998).
 - [6] B. B. Blinov *et al.*, *Quant. Inf. Proc.* **3**, 1 (2004).
 - [7] D. Kielpinski, C. Monroe, and D. J. Wineland, *Nature* **417**, 709 (2002).
 - [8] M. Rowe *et al.*, *Quantum Information & Computation* **2**, 257 (2002).
 - [9] K. Mølmer and A. Sørensen, *Phys. Rev. Lett.* **82**, 1835 (1999).
 - [10] E. Solano, R. L. de Matos Filho, and N. Zagury, *Phys. Rev. A* **59**, R2539 (1999).
 - [11] G. J. Milburn, S. Schneider, and D. F. V. James, *Fortschr. Physik* (2000).
 - [12] J. J. Garcia-Ripoll, P. Zoller, and J. I. Cirac, *Phys. Rev. Lett.* **91**, 157901 (2003).
 - [13] C. A. Sackett *et al.*, *Nature* **404**, 256 (2000).
 - [14] D. Leibfried *et al.*, *Nature* **422**, 412 (2003).
 - [15] P. C. Haljan *et al.*, *Phys. Rev. Lett.* **94**, 153602 (2005).
 - [16] P. J. Lee *et al.*, *quant-ph/0505203*.
 - [17] C. Langer *et al.*, *PRL* **95**, 060502 (2005).
 - [18] M. Paris and J. Rehacek, eds., *Quantum State Estimation*, vol. 649 of *Lect. Notes Phys.* (Springer-Verlag, 2004).
 - [19] D. F. V. James *et al.*, *Phys. Rev. A* **64**, 052312 (2001).
 - [20] C. F. Roos *et al.*, *Phys. Rev. Lett.* **92**, 220402 (2004).
 - [21] J. B. Altepeter, D. F. V. James, and P. G. Kwiat, *Lecture Notes in Physics* **649**, 113 (2004).
 - [22] D. Leibfried *et al.*, *Rev. Mod. Phys.* **75**, 281 (2003).
 - [23] D. M. Meekhof *et al.*, *Phys. Rev. Lett.* **76**, 1796 (1996).
 - [24] D. Leibfried *et al.*, *Phys. Rev. Lett.* **77**, 4281 (1996).
 - [25] A. Sørensen and K. Mølmer, *Phys. Rev. A* **62**, 022311 (2000).
 - [26] S. Wallentowitz and W. Vogel, *Phys. Rev. Lett.* **75**, 2932 (1995); S.-B. Zheng, *Phys. Rev. A* **58**, 761 (1998); H. Moya-Cessa, S. Wallentowitz and W. Vogel, *Phys. Rev. A* **59**, 2920 (1999); E. Solano *et al.*, *Phys. Rev. Lett.* **87**, 060402 (2001).
 - [27] The relative phases between the entangled states are chosen for simplicity since they do not affect the tomography.
 - [28] L. Deslauriers *et al.*, *Phys. Rev. A* **70**, 043408 (2004).
 - [29] P. J. Lee *et al.*, *Opt. Lett.* **28**, 1582 (2003).
 - [30] B. E. King *et al.*, *Phys. Rev. Lett.* **81**, 1525 (1998).
 - [31] J. J. Bollinger *et al.*, *Phys. Rev. A* **54**, R4649 (1996).

- [32] C. H. Bennett *et al.*, Phys. Rev. Lett. **76**, 722 (1996).
- [33] A. Stuart and J. K. Ord, *Kendall's Advanced Theory of Statistics*, vol. 1 (Oxford Univ. Press, 1987), 5th ed.
- [34] B. Efron and R. J. Tibshirani, *An Introduction to the Bootstrap* (Chapman & Hall, 1993).
- [35] A. Peres, Phys. Rev. Lett. **77**, 1413 (1996).
- [36] M. Horodecki, P. Horodecki, and R. Horodecki, Phys. Lett. A **223**, 1 (1996).
- [37] G. Vidal and R. F. Werner, PRA **65**, 032314 (2000).
- [38] J. Eisert and M. B. Plenio, J. Mod. Opt. **46**, 145 (1999).
- [39] M. B. Plenio and S. Virmani, quant-ph/0504163.
- [40] W. K. Wootters, Phys. Rev. Lett. **80**, 2245 (1998).
- [41] H. Häffner *et al.*, PRL **90**, 143602 (2003).
- [42] R. Ozeri *et al.*, PRL **95**, 030403 (2005).
- [43] K.-A. Brickman *et al.*, in preparation.